The Astrophysical Journal, 628:1023–1030, 2005 August 1

CORONAL LOOP HEATING BY NANOFLARES: THE IMPACT OF THE FIELD-ALIGNED DISTRIBUTION OF THE HEATING ON LOOP OBSERVATIONS

S. Patsourakos[1] and J. A. Klimchuk
Naval Research Laboratory, Space Science Division, Washington, DC 20375; patsourakos@nrl.navy.mil
Received 2004 August 19; accepted 2005 March 29

ABSTRACT

Nanoflares occurring at subresolution strands with repetition times longer than the coronal cooling time are a promising candidate for coronal loop heating. To investigate the impact of the spatial distribution of the nanoflare heating on loop observables, we compute hydrodynamic simulations with several different spatial distributions (uniform, loop top, randomly localized, and footpoint). The outputs of the simulations are then used to calculate density and temperature diagnostics from synthetic *TRACE* and SXT observations. We find that the diagnostics depend only weakly on the spatial distribution of the heating and therefore are not especially useful for distinguishing among the different possibilities. Observations of the very high temperature plasmas that are present only in the earliest stages of nanoflares can shed more light on the field-aligned distribution of the heating.

Subject headings: hydrodynamics — Sun: corona — Sun: magnetic fields

1. INTRODUCTION

Regions of enhanced magnetic flux on the Sun, active regions, are threaded by numerous coronal loops emitting in the extreme-ultraviolet (EUV) and soft X-ray (SXR). Coronal loops are ensembles of closed magnetic field lines loaded with hot and tenuous plasma. They are the main building blocks of active regions. The heating of these loops to temperatures of several MK represents a major unresolved problem of solar physics.

Recent space-borne missions (*Yohkoh*, *SOHO*, *TRACE*) have delivered data of unprecedented quality and led to a new picture of coronal loop structure and heating. Two of the most important new findings concern the densities and the thermal distribution of loops. First, coronal loops observed by *TRACE* and EIT at temperatures of $\approx$1–2 MK are overdense with respect to static equilibrium (e.g., Winebarger et al. 2003a; Aschwanden et al. 2001), whereas they are underdense when seen in hotter emissions ($T > 2$ MK) by SXT (Porter & Klimchuk 1995). The observations are also inconsistent with theoretical models of steady flows (Patsourakos et al. 2004). It would seem, therefore, that loops must be heated in a time-dependent fashion.

The second major finding, from spectroscopic observations, is that loops have broad differential emission measure distributions within their cross sections; i.e., they are multithermal (Schmelz et al. 2001; Martens et al. 2002). Given that heat transport is inefficient across magnetic field lines in the solar corona, this indicates that loops are comprised of subresolution magnetic strands. Evidently, each of the strands is heated impulsively and at different times from its neighbors. Although each strand evolves rapidly, the unresolved bundle that is the loop appears to change slowly compared to a cooling time (Winebarger et al. 2003b; Lopez-Fuentes et al. 2004).

Long ago, Parker (1988) introduced the idea of nanoflares, which are impulsive releases of roughly 10^{24} ergs of energy (some 9 orders of magnitude smaller than "normal" flares). He envisioned that random, slow motions of the footpoints of field lines in the photosphere make the magnetic field in the corona entangled and braided and increase its free energy. When the angle between adjacent misaligned flux strands reaches a threshold, perhaps related to the secondary instability (Dahlburg et al. 2003, 2005), a nanoflare occurs and releases a portion of the surplus energy.

If nanoflares are indeed of size 10^{24} ergs, and if coronal loops contain a large number of strands, as suggested by observations of elemental flux tubes in the photosphere, then the observed heating requirements of loops implies that the repeat time for successive nanoflares in a given strand must be longer than a cooling time. Cargill (1994), Cargill & Klimchuk (1997), and later Klimchuk & Cargill (2001) and Cargill & Klimchuk (2004) modeled the properties of loops in the context of this basic framework. They found that nanoflare-heated strands initially cool by thermal conduction and later cool by radiation. The first phase of cooling is characterized by underdensities relative to static equilibrium, and the second phase is characterized by overdensities (Klimchuk 2002, 2004; Warren et al. 2002; Spadaro et al. 2003; Cargill & Klimchuk 2004). Furthermore, because there are tens to thousands of strands, and because they are heated randomly, the observed ensemble can contain a broad range of temperatures at all times. These properties are consistent with the observations cited above. A critical aspect of this picture is that the nanoflare repetition time is long compared to a cooling time. If it were significantly shorter than a cooling time, each strand would be in a state of quasi-static equilibrium (e.g., Walsh et al. 1997; Mendoza-Briceño et al. 2002; Testa et al. 2005). This would be the case if the loop contained only a few strands, since the observed heating requirements imply a certain rate of 10^{24} erg nanoflares across the whole loop. The nanoflare model thus implies a high degree of cross-field spatial structure in the heating.

If the temporal envelope of the ensemble of nanoflares that occur within a coronal loop has a duration that exceeds the time, τ_{TRACE}, it takes a single strand to cool to *TRACE* temperatures ($\approx$1–2 MK), cotemporal and cospatial loop emission in *TRACE* and SXT should then be expected (e.g., Fig. 1). Therefore, each strand is heated several times by nanoflares. If, on the other hand, the envelope of nanoflares has a timescale that is comparable to or shorter than τ_{TRACE}, one would expect loops brightening first in SXT and then in *TRACE* (e.g., Schmieder et al. 2004; Winebarger & Warren 2005). However, there can be a transition period during which the loop would be visible in both instruments

[1] Also at Center for Earth Observing and Space Research, Institute for Computational Sciences, George Mason University, Fairfax, VA 22030.

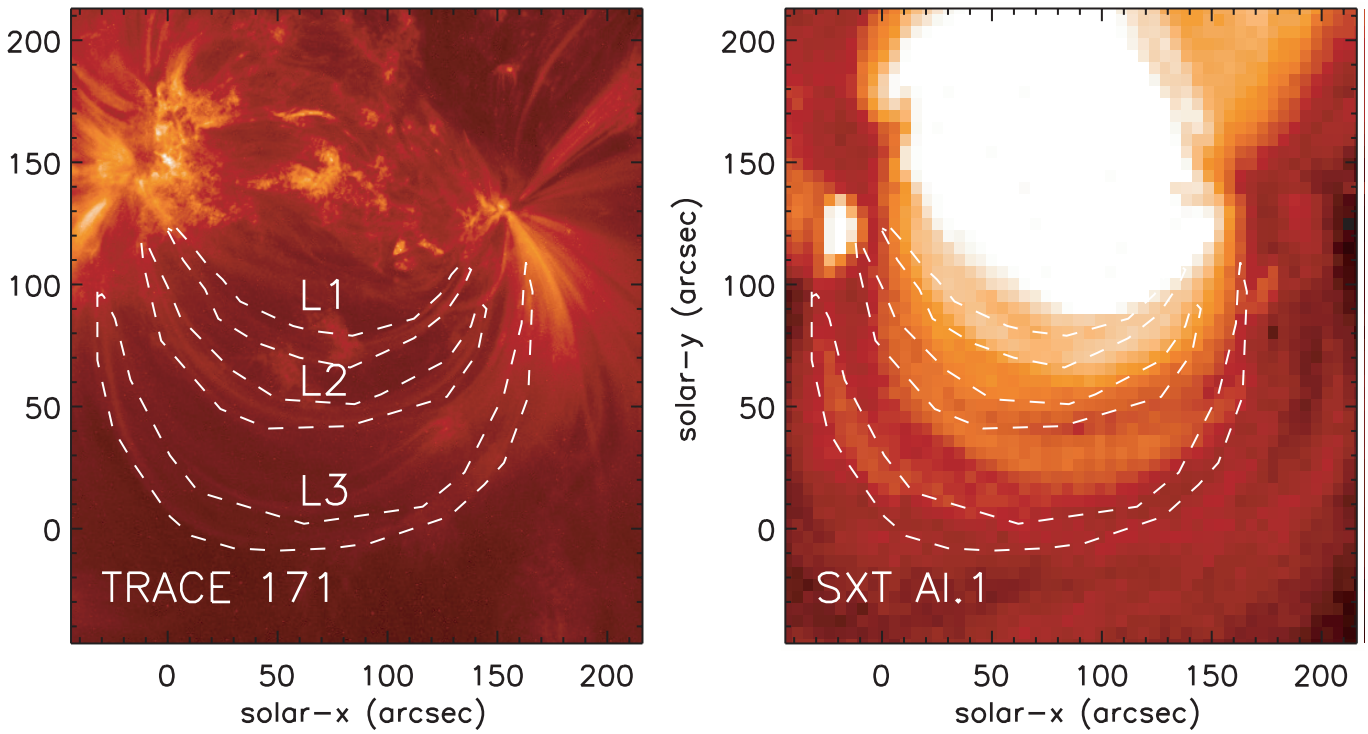

FIG. 1.—Co-aligned *TRACE* (171 Å) and SXT (Al.1) images of an active region taken on 2001 May 24. The images have a time difference of ≈10 minutes, and the uncertainty in the co-alignment is ≈6″ and 4″ in solar *x* and *y*, respectively. Three loop bundles (L1, L2, L3) were identified in the *TRACE* image. The boundaries of the three bundles are plotted with dashes on both images. L1 overlaps with an SXT loop along most of its length, while L2 and L3 only partially overlap with SXT loops.

corresponding to when it starts to dim in SXT and light up in *TRACE*. This means that each strand is heated only once by nanoflares. It is, however, currently unclear and debated whether SXT and *TRACE* loops correspond to exactly the same physical entity (e.g., Schmieder et al. 2004; Winebarger & Warren 2005). Figure 1 shows examples where SXT and *TRACE* loops do and do not appear to coincide.

Other evidence of subresolution structure comes from the work of Antiochos et al. (2003). They modeled a 5 MK equilibrium loop that cools after its heating is suddenly switched off. They showed that when the loop passes through 1 MK during the late cooling phase, its coronal section is nearly as bright in the *TRACE* 171 Å channel as are the transition region footpoints during the equilibrium and early cooling phases. The authors then examined an observed active region and found little evidence for distinct *TRACE* loops extending between the bright moss generally associated with transition region emission. They concluded that the heating must be steady. This conclusion is certainly correct, but only if the cross-field spatial scale of the heating is comparable to a typical loop diameter. If the scale is much smaller than a loop diameter, so that a loop contains many unresolved strands, then the heating can be impulsive. We note that the ratio of moss intensity to intermoss intensity observed by *TRACE* is accurately predicted by the nanoflare model, as we will show in a later paper. We also note that the nanoflare model predicts *TRACE* emission that is just as bright as observed. The emission measures (incorporating the corresponding filling factor) near 1 MK in the nanoflare model of Klimchuk & Cargill (2001, their Fig. 5) are similar to those of observed *TRACE* loops (e.g., Winebarger et al. 2003a).

Knowing the field-aligned spatial structure in the heating is also important, especially for constraining the possible physical mechanisms that produce the heating. Studies of "monolithic" loops (i.e., one large strand) have yielded conflicting results—that the heating is uniform along the loop (e.g., Priest et al. 1998), concentrated at the loop top (e.g., Reale 2002; Martens et al. 2002), concentrated at the loop footpoints (e.g., Antiochos et al. 1999; Aschwanden et al. 2001; Karpen et al. 2003; Patsourakos et al. 2004; Gudiksen & Nordlund 2005), and randomly localized along the loop (e.g., Galsgaard & Nordlund 1997). The situation is even less clear for multistranded loops heated by nanoflares. The purpose of our paper is to address this important issue. Our approach is to consider a comprehensive array of possible scenarios for the spatial dependence of nanoflare heating (uniform, random, loop top, footpoints). We perform hydrodynamic simulations and construct observables (densities and temperatures) as would be measured by instruments like *TRACE* and SXT. We then investigate the impact of the different spatial forms of the nanoflare heating on these observables. The key question we address is whether loop observations of this type reveal the spatial distribution of nanoflares along the magnetic field. Our paper is organized as follows: in § 2 we present the numerical model and give the details of the simulations, in § 3 we describe the *TRACE* and SXT nanoflare diagnostics obtained from the simulations, and finally in § 4 we discuss the results and give some conclusions.

2. NUMERICAL MODEL AND SIMULATIONS

Given the fact that the solar corona is a highly conducting low-β medium, the magnetic field confines the plasma within flux tubes, and the plasma can be described with one-dimensional hydrodynamics. The time-dependent single-fluid equations for conservation of mass, momentum, and energy along a coronal loop are

$$\frac{\partial \rho}{\partial t} + \frac{\partial}{\partial s}(\rho v) = 0, \tag{1}$$

$$\frac{\partial}{\partial t}(\rho v) + \frac{\partial}{\partial s}\left(\rho v^2\right) = \rho g_{\parallel}(s) - \frac{\partial P}{\partial s}, \quad (2)$$

$$\frac{\partial E}{\partial t} + \frac{\partial}{\partial s}[(E+P)v] = \rho v g_{\parallel}(s) - \frac{\partial F_{\rm heat}}{\partial s} - n^2\Lambda(T) + H, \quad (3)$$

and

$$E = \frac{1}{2}\rho v^2 + \frac{P}{\gamma - 1}, \quad (4)$$

where we have assumed that loops have a constant cross section, as supported by observations of both EUV and SXR loops (Watko & Klimchuk 2000; Klimchuk 2000). In the above equations, s corresponds to the distance along the loop from the "left" base of the model; $\rho = 1.67 \times 10^{-24} n$ is the mass density assuming a fully ionized hydrogen plasma with n being the electron number density; v is the plasma flow velocity; T is the plasma temperature; $P = 2nkT$ is the pressure from the ideal gas law; $\gamma = 5/3$ is the ratio of the specific heats; $F_{\rm heat}$ is the heat flux; H is the volumetric heating rate; $\Lambda(T)$ is the optically thin radiation loss function; and $g_{\parallel}(s)$ is the component of gravity parallel to the loop axis.

During intense impulsive energy releases, like nanoflares, the density increases much more slowly than the temperature. It is thus likely that the heat flux will saturate at a fraction of the free-streaming electron heat flux. As described in J. A. Klimchuk et al. (2005, in preparation), we account for this saturation by writing $F_{\rm heat}$ as a combination of the saturated heat flux, F_s, and the classical (collisional) Spitzer-Harm heat flux, F_c:

$$F_{\rm heat} = \frac{F_c F_s}{\sqrt{F_c^2 + F_s^2}}, \quad (5)$$

where

$$F_c = -\kappa_0 T^{5/2} \frac{\partial T}{\partial s}, \quad (6)$$

$$F_s = c\frac{3}{2} nk \left(\frac{k}{m}\right)^{1/2} T^{3/2} \frac{F_c}{|F_c|}. \quad (7)$$

In the above equations $\kappa_0 = 10^{-6}$ is the coefficient of thermal conduction, m is the electron mass, and c is a limiter, taken here as $\frac{1}{6}$. Our representation for $F_{\rm heat}$ assures a smooth transition between the extreme cases with either F_s or F_c dominating.

We take the heating rate, H, to be a separable function of s and time t:

$$H = h(s)g(t), \quad (8)$$

with $h(s)$ and $g(t)$ describing the spatial and temporal dependences, respectively.

The plane of the model loop is assumed to be perpendicular to the solar surface. The coronal part of our loop is taken to be semicircular with a full length $L = 150$ Mm, typical of observed loops. Attached to each end of the coronal semicircle is a 60 Mm chromospheric section. The total length of the model flux tube is therefore 270 Mm.

We adopt an optically thin radiative loss function $\Lambda(T)$ that has a piecewise continuous power-law form as given in Klimchuk & Cargill (2001). It is based on atomic physics calculations of J. Raymond (1994, private communication) and uses abundances that are a factor of 2 greater than the Meyer (1985) coronal values. The loss function drops precipitously to zero between 30,000 and 29,500 K, guaranteeing that the model chromosphere is approximately isothermal within this temperature range. A more realistic treatment would require optically thick radiative transfer and is unnecessary for studying the properties of the coronal part of the loop. All that we demand of the chromosphere is that it provide a source and sink of mass through the processes of chromospheric evaporation and condensation. Rigid wall boundary conditions are applied at the ends of the flux tube. Our model chromosphere is many gravitational scale heights thick [$H_g(T = 30{,}000\ {\rm K}) \approx 15$ Mm] so that the boundary conditions have negligible influence on the plasma dynamics in the transition region and corona and so that the height of the chromosphere is not affected by the depletion and accumulation of mass.

Equations (1)–(3) are solved using our state-of-art one-dimensional hydrodynamic code we call Adaptively Refined Godunov Solver (ARGOS), described in detail in Antiochos et al. (1999). ARGOS employs the PARAMESH parallel adaptive mesh refinement (AMR) package, which dynamically refines or derefines the grid based on the local density variations. PARAMESH allows us to track the small spatial scales associated with nanoflare dynamics, including propagating shocks and moving transition regions. It also allows us to impose highly localized heating at random locations along the loop. For the applications described in this paper, the minimum grid spacing is roughly 15 km. This does not fully resolve the very smallest scales that develop, but we found that decreasing the minimum grid space further does not qualitatively influence the results.

We began each simulation by first relaxing to a static equilibrium with uniform and steady heating. The peak temperature in the equilibrium was $\approx$2.5 MK. We then injected 20 successive nanoflares into the loop by applying a nonzero heating every 3800 s, which is longer than the plasma cooling time. Each nanoflare lasted 250 s with a heating rate that was constant in time [i.e., $g(t) \equiv 1$]. The uniform heating used to produce the initial equilibrium was turned off at the start of the first nanoflare and remained off for remainder of the simulation. Thus, the loop received no heating during the intervals between nanoflares. The 20 nanoflares had different energies covering a little over 1 order of magnitude. The energies were chosen such that the heating rate averaged along the loop varied randomly in the range 0.0006–0.01 ergs cm^{-3} s^{-1}. This corresponds to a total energy of roughly 10^{24} ergs for a cross-sectional area of 100×100 km^2. The "loop" in our simulations is therefore formerly equivalent to one of the subresolution strands that, together, make up an observed "macroscopic" loop.

What differentiates the nanoflare models of this work from earlier studies is the *spatial* distribution of the nanoflare heating. We considered six different forms for $h(s)$, corresponding to a comprehensive array of spatial distributions of the heating. They are

$$h(s) = \begin{cases} H_0 & \text{model A (uniform)} \\ H_1 \exp\left[-\left(\dfrac{s - s_0}{\sigma_{H_1}}\right)^2\right] & \text{model B (random)} \\ H_2 \exp\left[-\left(\dfrac{s - s_0}{\sigma_{H_2}}\right)^2\right] & \text{model C (random)} \\ H_1 \exp\left[-\left(\dfrac{s - s_{1/2}}{\sigma_{H_1}}\right)^2\right] & \text{model D (top)} \\ H_3 \left\{ \exp\left(-\dfrac{s - s_1}{\sigma_{H_3}}\right) + \exp\left[\dfrac{s - (s_1 + L)}{\sigma_{H_3}}\right] \right\} & \text{model E (footpoints)} \\ H_4 \exp\left(-\dfrac{s - s_1}{\sigma_{H_3}}\right) & \text{model F (asymmetric),} \end{cases} \quad (9)$$

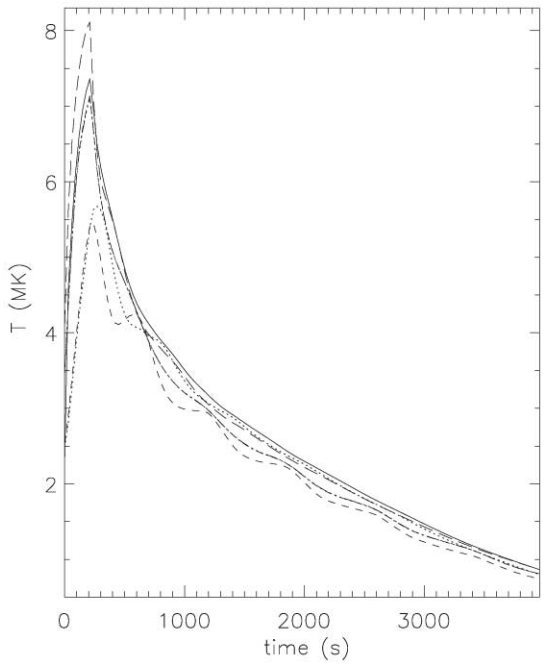

FIG. 2.—Average temperature over the upper $\frac{2}{3}$ of the loop as a function of time for the first nanoflare for model: A: solid line, B: dash–double-dotted line, C: dash-dotted line, D: long-dashed line, E: dotted line, and F: dashed line.

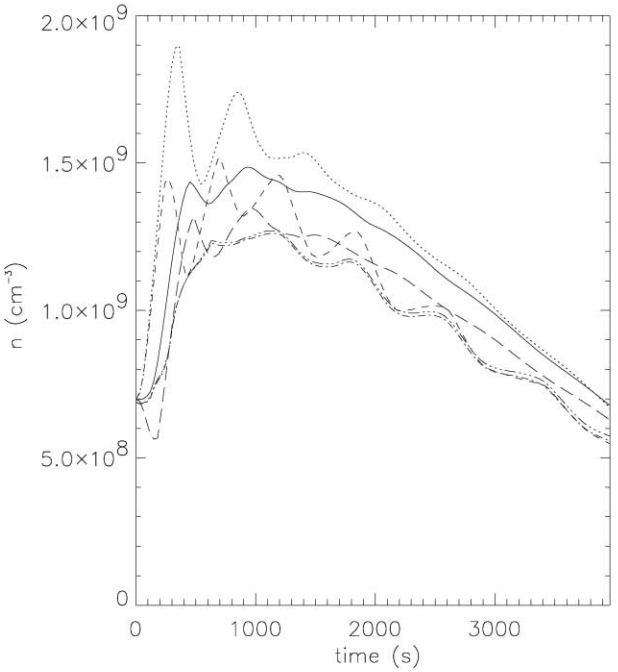

FIG. 3.—Same as Fig. 2, but for density.

and were inspired by the various results on the spatial distribution of coronal heating given in § 1. In the above equation s_0 is a random location along the coronal section of the loop, $s_{1/2}$ is the location of the loop apex, s_1 is the initial ($t = 0$) position of the base of the corona (top of the chromosphere) in the left footpoint of the loop. Also, $\sigma_{H_1} = 0.5$ Mm, $\sigma_{H_2} = 2.5$ Mm, and $\sigma_{H_3} = 10$ Mm. The nanoflare heating was therefore uniform in space for model A, localized at random coronal positions for models B and C (identical positions for the two cases, but 5 times more localized for B), localized at the loop apex for model D, localized at both footpoints for model E, and localized at only the left footpoint for model F. The length scale of the heating was much smaller than the loop length in all of the nonuniform cases. The heating magnitudes (i.e., H_0, H_1, H_2, H_3, H_4) were chosen in such a way that the total heating going to the coronal part of the loop (i.e., excluding the chromosphere) was the *same* for all models. This total energy varied from one nanoflare to the next, but it varied in the same way for each of the models.

All of our nanoflare simulations followed the same generic pattern of impulsively heated loops found by previous studies: chromospheric evaporation during the heating phase and the initial conductive cooling phase, followed by draining and condensation during the later radiative cooling phase. Figures 2 and 3 show the evolution of the spatially averaged temperature and density (averaged along the upper $\frac{2}{3}$ of the loop) for the first nanoflare. Early on, the models with footpoint heating (E and F) have lower temperatures and higher densities than do the other models (see also Peres et al. 1983; Tsiklauri et al. 2004). The reason for the lower temperatures is that the initial response to the impulsive heating is to raise the temperature locally. A given energy input will raise the temperature of a high-density (low-altitude) plasma less than it will raise the temperature of a low-density (high-altitude) plasma. The reason for the more rapid density increase has to do with the initial temperature gradients that develop. Although the temperature enhancement is smaller in models E and F, it occurs at lower altitudes, resulting in a steeper gradient and larger conductive flux into the chromosphere. Chromospheric evaporation is correspondingly enhanced, and the coronal density increases more rapidly.

After the nanoflare ends, the differences among the models decrease. Thermal conduction and mass flows tend to smooth out any temperature structure that was produced by localized heating. The oscillatory behavior that is present in Figures 2 and 3 is due to waves, often shocked, that are initiated by the nanoflare and propagate back and forth along the loop. A similar phenomenon is likely responsible for the oscillating Doppler shifts observed in very hot (>6 MK) loops by SUMER (e.g., Wang et al. 2002).

3. *TRACE* AND SXT DIAGNOSTICS

From each of our models, we simulated the observation of a multistranded loop. Although each model represents the evolution of a single strand, we assumed that the states of the strand at 250 randomly selected times can be used to represent 250 independent strands observed at the same time. Using the temperature response functions for the *TRACE* 171 and 195 Å channels and the SXT thin Al and AlMg channels, we computed the intensities as a function of position for each of the 250 times. We then averaged the intensities over the upper $\frac{2}{3}$ of the loop, to avoid the bright moss emission from the footpoints (e.g., Martens et al. 2000; Antiochos et al. 2003). We next summed the intensities for the 250 times, giving us a simulated snapshot observation of the corona in a single multistranded loop. Finally, we used the standard filter ratio method to compute a *TRACE* temperature and density from the 171 and 195 Å intensity pair and an SXT temperature and density from the thin Al and AlMg intensity pair. This is the same method commonly applied to actual observations (e.g., Porter & Klimchuk 1995; Aschwanden et al. 1999, 2000; Winebarger et al. 2003a). Note that it assumes the loop volume is completely filled with an isothermal constant-density plasma (i.e., filling factor 1), even though the plasma is actually characterized by a broad distribution of temperatures and densities.

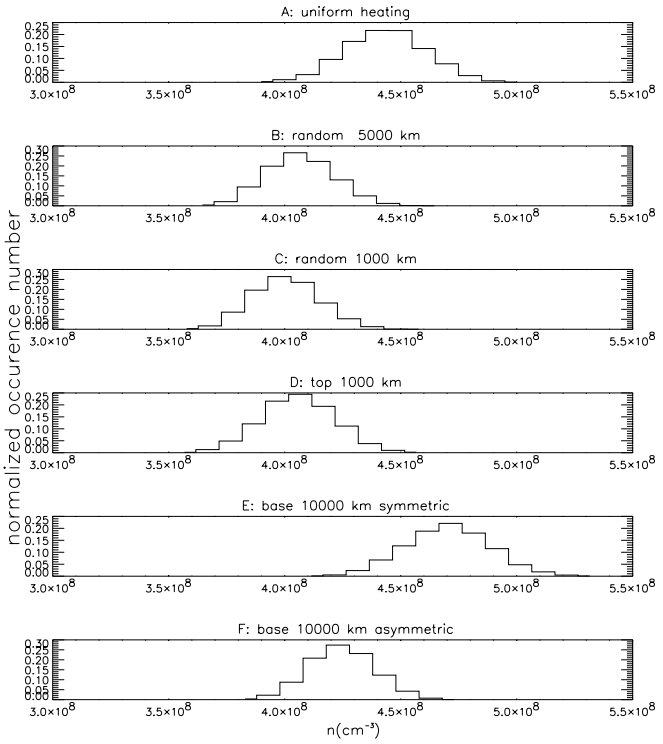

FIG. 4.—Distributions of *TRACE* densities for 250 random times for models A–F (*top to bottom*).

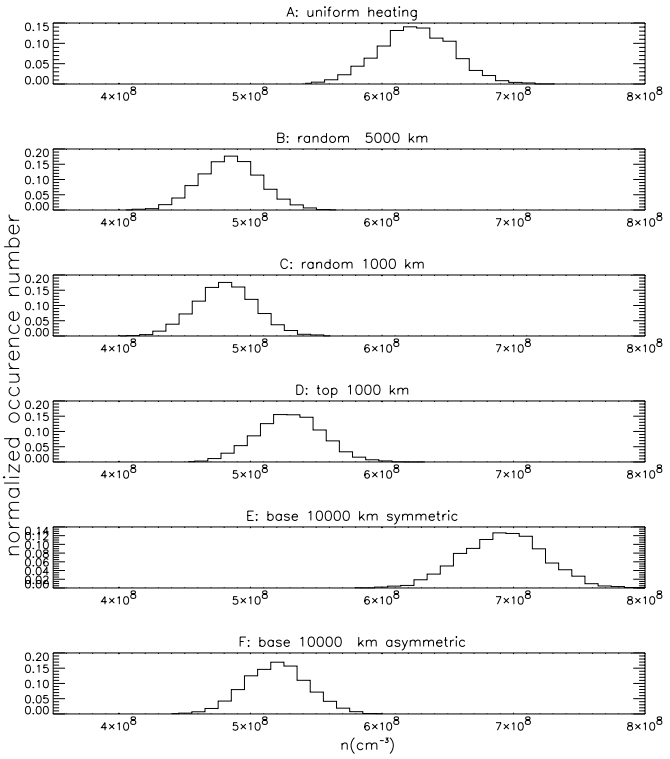

FIG. 5.—Same as Fig. 4, but for SXT densities.

We repeated the above procedure 5000 times for each of our models. Figures 4 and 5 show the resulting density distributions for the simulated *TRACE* and SXT observations, respectively. Figure 6 shows the SXT temperature distributions. The *TRACE* temperature distributions are very sharply peaked near 1.2 MK and are not shown. We see that the differences among the models are very small. All of the distributions are quite narrow, with full widths at half maximum of less than 10%. The peaks of the distributions, which represent the most probable values, deviate by only ≈20% and 30% for the *TRACE* and SXT densities and by only ≈3% and 5% for the *TRACE* and SXT temperatures, respectively. Model E (symmetric footpoint heating) has the largest densities, while model C (randomly localized heating) has the smallest. Model A (uniform heating) has the highest temperatures, while model D (looptop heating) has the lowest. The SXT densities are a factor of 4 smaller than predicted by static equilibrium theory using SXT temperatures, and the *TRACE* densities are a factor of 4 larger than predicted by the theory using *TRACE* temperatures. This is consistent with actual observations, as discussed in § 1.

The simulated observations we have just described are appropriate to long-lived loops in which the nanoflares repeat multiple times in each strand. We would expect such loops to appear bright in SXT and *TRACE* at the same time. However, as discussed in § 1, this is often not the case. It is more typical for distinct loops to be seen first in SXT and later in *TRACE*, sometimes with a period of overlap. For these loops, the envelope of the nanoflares must be shorter than $\tau_{TRACE} \approx 2000$ s. We investigate this different situation by considering 500 s time intervals during the first nanoflare event in each sequence. We average the SXT and *TRACE* emission over these intervals (and over the upper $\frac{2}{3}$ of the loop) and thereby simulate observations of a multistranded loop in which each strand is heated only once and in which the envelope of nanoflares is only 500 s. Because an actual loop may be observed at an time after the start of the envelope, we examine the intervals [0, 500], [500, 1000], [1000, 1500] s, etc. SXT and *TRACE* densities and temperatures are inferred for each interval using the filter-ratio method, as before. We find that the different spatial distributions of the nanoflares lead to only small differences in the inferred quantities. The maximum

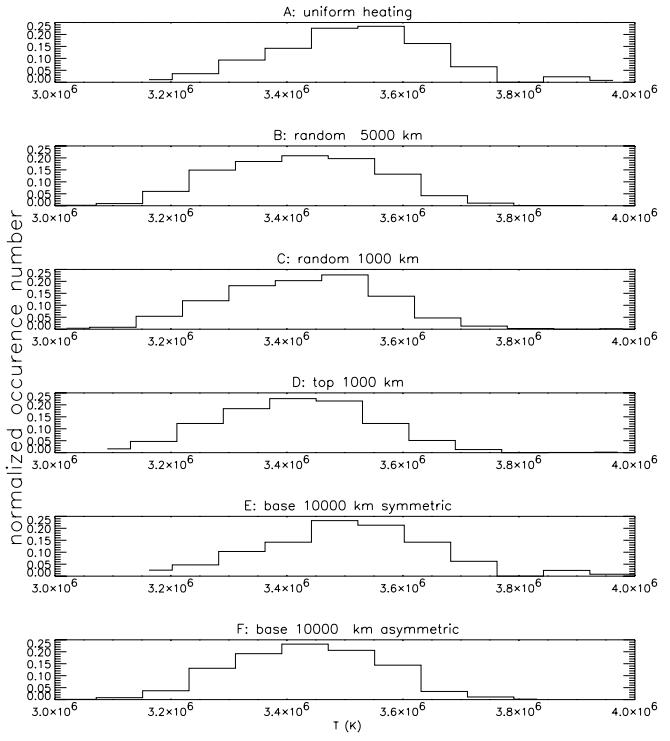

FIG. 6.—Same as Fig. 4, but for SXT temperatures.

deviations are ≈30% and 40% for the *TRACE* and SXT densities, respectively, and ≈2% for *TRACE* and SXT temperatures.

4. CONCLUSION AND DISCUSSION

The results of the previous section indicate that plasma diagnostics using *TRACE* and SXT depend only weakly on the spatial distribution of nanoflare heating. They also do not depend on whether nanoflares occur over a finite interval of time within the loop or indefinitely. It is therefore difficult to infer the distribution from such observations. A similar conclusion was reached by Winebarger & Warren (2004), who found that the apex density of an impulsively heated loop, when seen in *TRACE* temperatures, does not depend on the position along the loop where the heating is concentrated.

The main reason for the weak dependence is related to the fact that SXT and *TRACE* intensities are dominated by emissions produced during the cooling of the strands, long after the nanoflare has occurred. *TRACE* is insensitive to the initial hot temperatures. SXT is sensitive to these temperatures, but the densities and emission measures are small until chromospheric evaporation has had time to fill the loop. The temperature profiles of the different heating models are quite distinct in the early stages. However, thermal conduction and mass flows (via the enthalpy flux) are very efficient at redistributing the energy along the strand, so the initial differences are rapidly smoothed out. In essence, the loop loses memory of the spatial distribution of the heating. This is illustrated in Figures 7, 8, and 9, which show the temperature profiles of the different models at times of 60, 1200, and 3000 s after the start of the first nanoflare. At the latter two times the peak temperature is ≈3 and 1.5 MK, typical of SXT and *TRACE* observations, respectively. The profiles of the different models are qualitatively different in Figure 7, but not in Figures 8 and 9. It would be difficult to distinguish among the models in a spatially resolved strand, except possibly early in the event when the strand is comparatively faint. It would be even more difficult to make a distinction in a complete loop comprised of large number of unresolved strands.

The actual number of strands in a real loop is not known, although observations of elemental flux tubes in the photosphere suggest it is quite large. To investigate the sensitivity of our results to the number of strands, we have repeated our analysis using

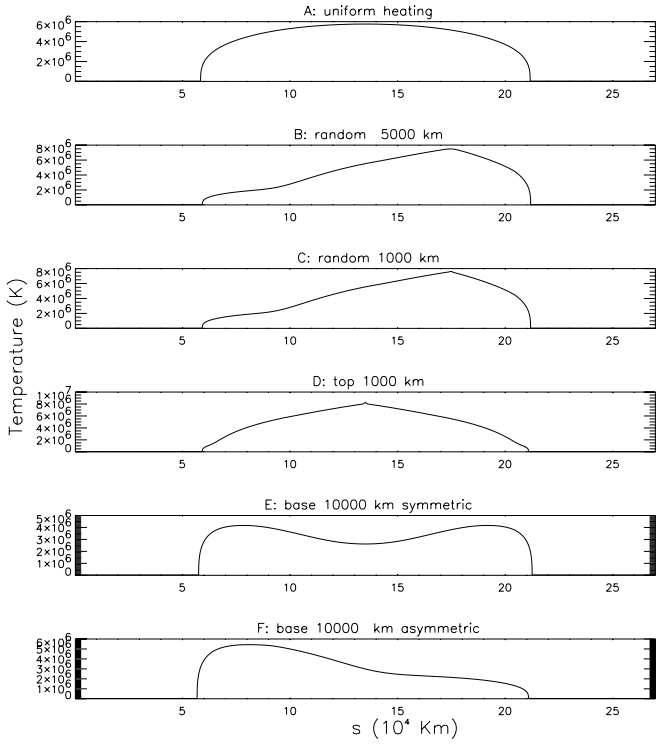

FIG. 7.—Temperature along the loop, 60 s after the start of the first nanoflare, for models A–F (*top to bottom*).

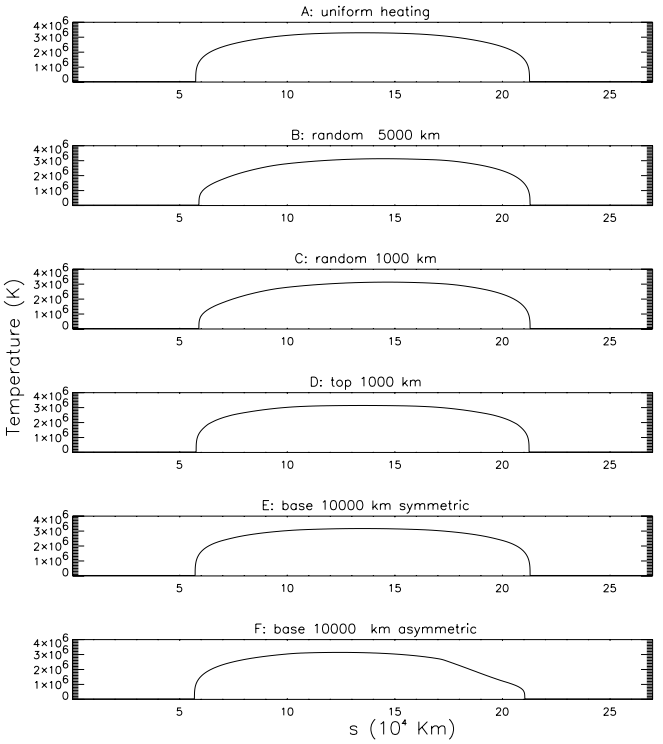

FIG. 8.—Same as Fig. 7, but at 1200 s after the start of the first nanoflare.

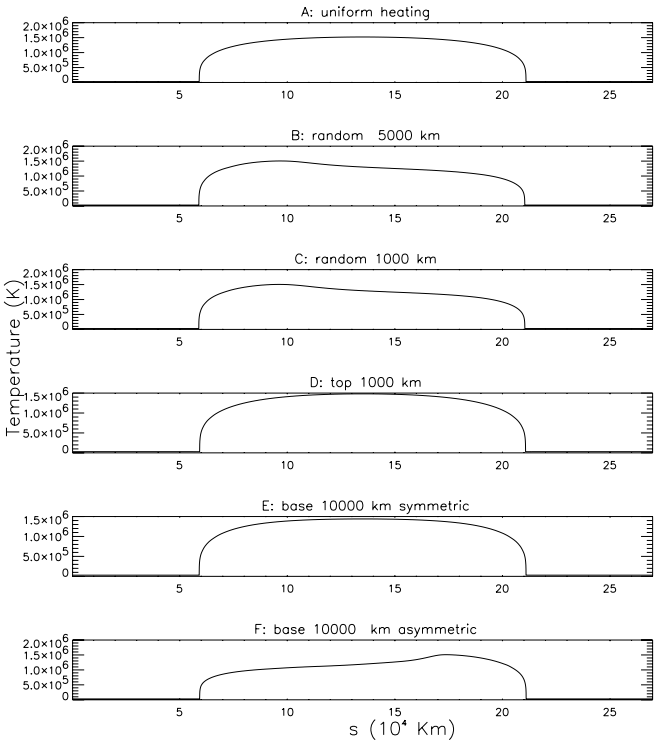

FIG. 9.—Same as Fig. 7, but at 3000 s after the start of the first nanoflare.

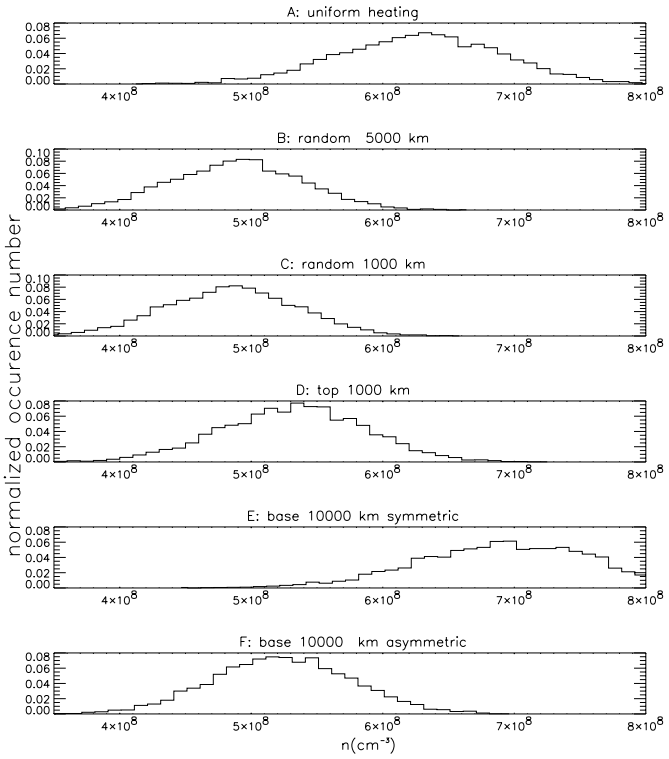

FIG. 10.—Distributions of the SXT densities for 50 random times for models A–F (*top to bottom*).

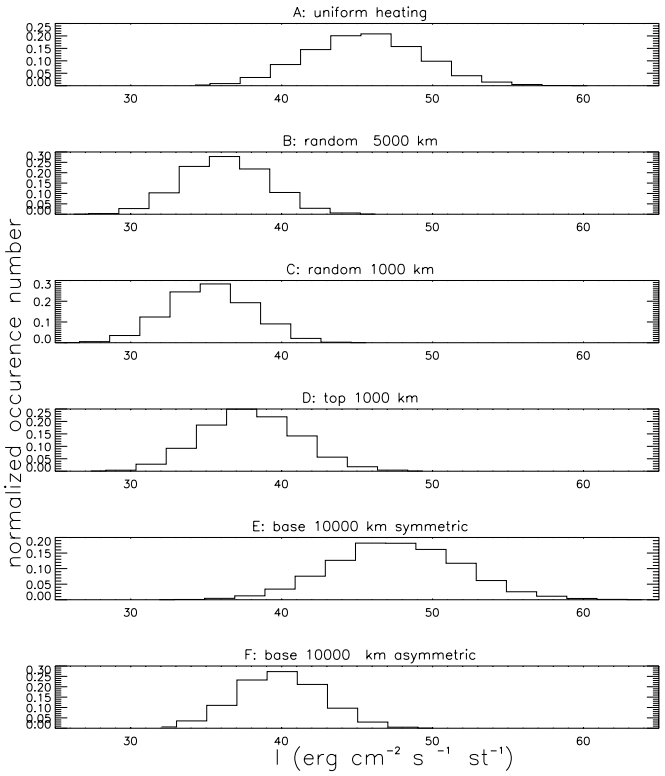

FIG. 11.—Distributions of the intensities for the Fe XII lines at ≈195 Å for 250 random times for models A–F (*top to bottom*).

50 random times, instead of 250, to assemble our "snapshot" of a multistranded loop. The resulting SXT density distributions are shown in Figure 10. The changes in the distributions are quite minor (see Fig. 5). The distributions are about twice as broad, but the peaks occur at nearly the same places.

The SXT instrument is very broad band, i.e., sensitive to a wide range of wavelengths and temperatures. The band of *TRACE* is much narrower, but it nonetheless includes several spectral lines formed at different temperatures. We have therefore considered the diagnostic potential of spectral lines formed at the same temperature. Figure 11 shows the distribution of intensities obtained from simulated observations of the 195.12 and 195.13 Å lines of Fe XII, formed at ≈1.25 MK. The distributions were constructed the same way as before, using 250 random times. As with the *TRACE* and SXT diagnostics, the intensities do not differ substantially among the different heating models. The maximum difference in the distribution peaks is ≈30%.

In closing, we note that the best way to study the field-aligned spatial distribution of nanoflare heating is to observe the very high temperature plasmas that are present only in the earliest stages of an event. Such observations should be available when the Extreme-ultraviolet Imaging Spectrometer (EIS) is launched on *Solar-B*.

We thank the referee Piet Martens for several very enlightening comments and suggestions on the manuscript. Research supported by NASA and ONR.

REFERENCES

Antiochos, S. K., Karpen, J. T., DeLuca, E. E., Golub, L., & Hamilton, P. 2003, ApJ, 590, 547
Antiochos, S. K., MacNeice, P. J., Spicer, D. S., & Klimchuk, J. A. 1999, ApJ, 512, 985
Aschwanden, M. J., Newmark, J. S., Delaboudinière, J.-P., Neupert, W. M., Klimchuk, J. A., Gary, G. A., Portier-Fozzani, F., & Zucker, A. 1999, ApJ, 515, 842
Aschwanden, M. J., Nightingale, R. W., & Alexander, D. 2000, ApJ, 541, 1059
Aschwanden, M. J., Schrijver, C. J., & Alexander, D. 2001, ApJ, 550, 1036
Cargill, P. J. 1994, ApJ, 422, 381
Cargill, P. J., & Klimchuk, J. A. 1997, ApJ, 478, 799
———. 2004, ApJ, 605, 911
Dahlburg, R. D., Klimchuk, J. A., & Antiochos, S. K. 2003, Adv. Space Res., 32, 1029
———. 2005, ApJ, 622, 1191
Galsgaard, K., & Nordlund, A. 1997, J. Geophys. Res., 102, 219
Gudiksen, B., & Nordlund, A. 2005, ApJ, 618, 1020
Karpen, J. T., Antiochos, S. K., Klimchuk, J. A., & MacNeice, P. J. 2003, ApJ, 593, 1187
Klimchuk, J. A. 2000, Sol. Phys., 193, 53
Klimchuk, J. A. 2002, Inst. for Theoretical Physics Conference on Solar Magnetism and Related Astrophysics, ed. G. Fisher & D. Longcope (Santa Barbara: Univ. California) (http://online.kitp.ucsb.edu/online/solar_c02/klimchuk)
———. 2004, Proceedings of the *SOHO*-15 Meeting on Coronal Heating, ed. R. Walsh & J. Ireland (ESA SP-575; Noordwijk: ESTEC), 2
Klimchuk, J. A., & Cargill, P. J. 2001, ApJ, 553, 440
Lopez Fuentes, M. C., Mandrini, C. H., & Klimchuk, J. A. 2004, BAAS, 204, 5602
Martens, P. C. H., Cirtain, J. W., & Schmelz, J. T. 2002, ApJ, 577, L115
Martens, P. C. H., Kankelborg, C. C., & Berger, T. E. 2000, ApJ, 537, 471
Mendoza-Briceño, C. A., Erdélyi, R., & Sigalotti, L. D. G. 2002, ApJ, 579, L49
Meyer, J. P. 1985, ApJS, 57, 173
Parker, E. N. 1988, ApJ, 330, 474
Patsourakos, S., Antiochos, S., & Klimchuk, J. A. 2004, ApJ, 614, 1022
Patsourakos, S., Klimchuk, J. A., & MacNeice, P. J. 2004, ApJ, 603, 322
Peres, G., et al. 1983, ApJ, 270, 270
Porter, L. J., & Klimchuk, J. A. 1995, ApJ, 454, 499
Priest, E. R., Foley, C. R., Heyvaerts, J., Arber, T. D., Culhane, J. L., & Acton, L. W. 1998, Nature, 393, 545
Reale, F. 2002, ApJ, 580, 566

Schmelz, J. T., Scopes, R. T., Cirtain, J. W., Winter, H. D., & Allen, J. D. 2001, ApJ, 556, 896
Schmieder, B., Rust, D. M., Georgoulis, M. K., Demoulin, P., & Bernasconi, P. N. 2004, ApJ, 601, 530
Spadaro, D., Lanza, A. F., Lanzafame, A. C., Karpen, J. T., Antiochos, S. K., Klimchuk, J. A., & MacNeice, P. J. 2003, ApJ, 582, 486
Testa, P., Peres, G., & Reale, F. 2005, ApJ, 622, 695
Tsiklauri, D., Aschwanden, M. J., Nakariakov, V. M., & Arber, T. D. 2004, A&A, 419, 1149
Walsh, R. W., Bell, G. E., & Hood, A. W. 1997, Sol. Phys., 171, 81
Wang, T. J., Solanki, S. K., Curdt, W., Innes, D. E., & Dammasch, I. E. 2002, ApJ, 574, L101
Warren, H. P., Winebarger, A. R., & Hamilton, P. S. 2002, ApJ, 579, L41
Watko, J. A., & Klimchuk, J. A. 2000, Sol. Phys., 193, 77
Winebarger, A. R., & Warren, H. P. 2004, ApJ, 610, L129
———. 2005, ApJ, 626, 543
Winebarger, A. R., Warren, H. P., & Mariska, J. T. 2003a, ApJ, 587, 439
Winebarger, A. R., Warren, H. P., & Seaton, D. B. 2003b, ApJ, 593, 1164